Contents lists available at ScienceDirect

Environment International

Full length article

Arsenic release from arsenopyrite weathering in acid mine drainage: Kinetics, transformation, and effect of biochar

Ling Cen [a,c], Hongguang Cheng [b], Qingyou Liu [a,*], Shuai Wang [a,c], Xi Wang [b,c]

[a] *Key Laboratory of High-temperature and High-pressure Study of the Earth's Interior, Institute of Geochemistry, Chinese Academy of Sciences, Guiyang 550081, China*
[b] *State Key Laboratory of Environmental Geochemistry, Institute of Geochemistry, Chinese Academy of Sciences, Guiyang 550081, China*
[c] *University of Chinese Academy of Sciences, Beijing 100039, China*

ARTICLE INFO

ABSTRACT

Arsenopyrite (FeAsS) oxidative dissolution provides an important source for the occurrence of high arsenic in acid mine drainage (AMD). Biochar is a potent material that can dramatically sequestrate an array of heavy metals in water. However, little is known about the role of biochar on the fate of As from arsenopyrite in AMD. This study investigates the effects of biochar concentrations, AMD acidities, and temperatures on the release of As from arsenopyrite in a simulated AMD over a range of environmentally relevant conditions. Results show that biochar inhibits As release and further acidification without changing the arsenopyrite weathering mechanism. Arsenopyrite is first oxidized to Fe(II), As(III) and S^0 and ultimately oxidized to Fe(III), As(V) and SO_4^{2-}, respectively. Higher concentration, temperature or higher acidity promotes the arsenic release rate. Electrochemical studies showed that biochar inhibited As release and acidification for reduced the charge transfer resistance at the double layer and film resistance at the passivation layer, which was mainly attributed to Fe(III) ions in AMD being adsorbed, oxidized, and As complexed to biochar-Fe-As(V). This study reveals the release mechanism of As from arsenopyrite weathering in AMD and suggests the applicability of biochar in mitigating arsenic pollution and further acidification in sulfide mineral mine drainage.

1. Introduction

Water arsenic (As) contamination is a global environmental problem (Lombard et al., 2021). Podgorski et al. (2017) estimated that approximately 150 million people around the world are at the risk of arsenic-contaminated groundwater water. The release of As from arsenic-bearing mines through geological and anthropogenic processes is the major source of high arsenic in the water (Rajpert et al., 2016; Rebello et al., 2021; Tabelin et al., 2021). Arsenopyrite (FeAsS) is the most common As-bearing mineral, which broadly distribute in mineralized areas (Tabelin et al., 2020, 2021), also distribute in groundwater and civil works for resource utilization (Huyen et al., 2019; Park et al., 2019), and its oxidation is the widespread mechanism for the distribution of arsenic into the environment (Flora, 2015). In the Alexander mine (New Zealand), the As-enriched tailings comprise a ~1m thick package of finely laminated (mm-scale) sediments, which results in the tailings sediments being As-rich (up to 5000 mg·kg^{-1}) due to relict arsenopyrite and As-bearing pyrite (Tay et al., 2021). In Snow Lake (Canada), there are approximately 250,000 tons of cyanide-treated,

refractory arsenopyrite ore concentrate. As released to pore water during the oxidation of arsenopyrite and other sulfide minerals, adjacent water has concentrations of >20 mg·L^{-1} As(T) (Salzsauler et al., 2005). Consequently, there is increasing public concern about arsenic contamination in water from arsenopyrite and provides important implications for the prevention and control of As pollution in mine drainage (Genc-Fuhrman et al., 2005; Hong et al., 2021).

As a semiconducting mineral, the process of arsenopyrite oxidizing and releasing arsenic is an electron transfer process, i.e., it is an electrochemical process in nature. Consequently, many studies have been carried out to understand the arsenic release mechanism of arsenopyrite oxidation depending on electrochemical techniques. Fernandez et al. (1996) confirmed that arsenopyrite can be oxidized in dilute acid and that the oxidation was controlled by an electrochemical surface reaction step with an apparent activation energy of 33 kJ·mol^{-1}. Then, Lázaro et al. (1997) further revealed that the oxidation of arsenopyrite in acidic media first produced As$_2$S$_2$ and Fe^{2+} and subsequently transformed to H$_3$AsO$_4$ and Fe^{3+}. However, the intermediate process of the above transformation is still controversial, i.e., they may elemental sulfur,

polysulfides, metal-deficient sulfide $Fe_{1-x}As_{1-y}S$ or As-S groups (Buckley and Walker, 1988; Costa et al., 2002; McGuire et al., 2001). With the development of synchrotron-based radiation technology, Mikhlin and Tomashevich (2005) confirmed an As- and Fe-rich overlayer with an S-enriched layer of arsenopyrite oxidized in acidic solutions by synchrotron X-ray absorption near the edge structure. To natural conditions, previous studies have shown that the presence of strong oxidants (Ma et al., 2014), the pH of environmental media (Lara et al., 2016), ions with the ability to penetrate or complexate (Zheng et al., 2020), phosphate (Park et al., 2021), metal–organic complexes (Park et al., 2018) and organic matter (Wang et al., 2021) all affect arsenic release and transformation from arsenopyrite weathering. In arsenopyrite mines, acid mine drainages (AMDs) are broadly distributed, and the source determines that AMDs contain many Fe^{3+} ions (She et al., 2021). In contrast, the numerous strongly oxidizing Fe^{3+} ions in AMD will greatly influence arsenic release (McKibben et al., 2008), including more phase transitions from arsenopyrite oxidation (Neil and Jun 2015). However, the mechanism of arsenic release, especially the thermodynamic and kinetic data of arsenopyrite oxidation in AMD remains unknown.

In recent years, many studies have shown that biochar is an excellent material for repairing heavy metal pollution in water and soil (Ahmad et al., 2014; Yang et al., 2020), due to the large specific surface area, high porosity, strong ion exchange capacity, and complexation with oxygen-containing functional groups (Zhang et al., 2020a). For the removal of arsenic, biochar may not be an ideal absorbent because most biochar are negatively charged (Yaashikaa et al., 2019). In certain water environments, biochar is a potential absorbent for the oxidation and fixation of As(III) (Niazi et al., 2018). Because AMD has arsenic and a high concentration of Fe^{3+} ions, Fe^{3+} ions may obviously be adsorbed by biochar. With metal sulfide mineral resources are exploited, transferred and utilized, more and more arsenopyrite enter into the soil and water around the mining area, even around metallurgical refinery, resulting in high arsenic-contaminated, acidic drainage and heavy metal pollution. Due to forest fires (Preston and Schmidt, 2006), especially biochar is widely used in environmental pollution improvement (Veselska et al., 2022; El-Naggar et al., 2021), there are many natural environments in which arsenopyrite and biochar coexist. However, whether arsenic ions may complex with biochar or complex with biochar via Fe^{3+} ions remains unknown.

The objectives of this study are therefore to determine to what extent and how biochar influences the fate and transport of As during the oxidation of arsenopyrite in AMD. For these purposes, the effects of biochar concentration, environmental temperature and the acidity of AMD on As release were explored during arsenopyrite oxidation by different electrochemical and surface analysis measurements. Understanding the mechanism of As release from arsenopyrite oxidation in the presence of biochar at AMD conditions can supplement the knowledge of As geochemical cycling in AMD, and provide optimized biochar usage for acidic drainage for the remediation and management of As-bearing sites affected by mining activities.

2. Materials and methods

2.1. Arsenopyrite electrode, biochar and AMD preparation

Arsenopyrite specimens were obtained from the Xingwen mine of Sichuan Province, China. X-ray diffraction (Empyrean, Panaco of Netherlands) indicated that the selected minerals were pure and homogeneous (Fig. S1). Electron microprobes showed that they mainly consisted of Fe 34.28 %, As 46.44 % and S 18.96 % (wt. %). Block specimens were selected as working electrode. First, they were cut into $0.5 \times 0.5 \times 0.9$ cm^3 cuboids. Then, the cube upper surface was attached to a copper conductor with silver paint, while the rest was sealed with epoxy resin, exposing only the lower surface in contact with the electrolyte. Muñoz et al. (1998) showed the detailed and specific electrode fabrication method.

The source of the biochar used in this experiment was straw. After oven drying at 80 °C for 24 h, the raw material was cut into thin slices of 10 cm and placed in a muffle oven to heat to 550 °C at a rate of 20 °C per min. After keeping the raw material warm for an hour, slow pyrolysis was used to transform it into biochar. The biochar was then ground and screened to obtain a sample with a particle size of 200 meshes. The sample was then put into an oven and dried at 105 °C to obtain a constant weight. The physical and chemical properties of the obtained biochar are shown in Table S1, which has a 10.5 m^2·g^{-1} specific surface area. The biochar has a 19.98 Å pore size and its detailed porosities by N$_2$ adsorption isotherm are shown in Table S2, and the pore size distribution by NLDFT are shown in Fig. S2. The preparation of biochar has been provided in Cheng et al. (2017). Acid mine drainage (AMD) was collected from the Xingwen mine of Sichuan Province, China. The AMD was first filtered with a 0.45 μm membrane, then, it was boiled in an airtight container for 3 h to sterilize acidophilic microorganism. The AMD mainly consisted of Fe^{3+}, Fe^{2+}, SO_4^{2-} and Cl$^-$ at a pH of 2.99. To investigate the influence of acidity, H$_2$SO$_4$ and NaOH solutions were used to obtain pH 1.99, pH 3.99 and pH 4.99 (Table S3). Meanwhile, the prepared biochar was added to the AMD solution at varying weights to obtain AMD solutions with varying concentrations of biochar (0.4 g·L^{-1}, 0.8 g·L^{-1} and 1.2 g·L^{-1}).

2.2. Immersion experiments

Eight block arsenopyrite specimens (each 0.5 cm × 0.5 cm × 0.05 cm, sealed with epoxy resin exposing only one surface) and eight-arsenopyrite powder specimens (each 0.3 g) were divided into two groups. Then, they were dipped into 60 mL AMD with different concentrations of biochar (0 g·L^{-1}, 0.4 g·L^{-1}, 0.8 g·L^{-1} and 1.2 g·L^{-1}) for 2 months. The volume of the reactor is 100 mL, and 2 mL of solution was collected in each reactor during sampling to detect various ions in the solution. The Zeta potential of the AMD solution at different concentrations of biochar or arsenopyrite are shown in Table S4. Prior to the immersion experiments, the block arsenopyrite specimens were polished with silicon carbide sandpaper (1000, 3000, 5000 mesh) to obtain a mirror-like surface, then, degreased using alcohol, cleaned ultrasonically using deionized water and dried in nitrogen. The arsenopyrite powder specimens were crushed and ground to 200 mesh using an agate mortar and pestle with an alcohol solvent, then dried in nitrogen.

2.3. Characterization and analysis

The eroded block arsenopyrite specimens were studied using scanning electron microscopy (SEM) (JSM-6460LV) (JEOL ltd.), and energy dispersive spectroscopy (EDS) (Oxford Instruments Co.). The eroded power arsenopyrite specimens were characterized by Raman spectroscopy (British Renishaw) and Fourier transform infrared spectroscopy (FTIR). The As and S speciation transformations on the arsenopyrite surfaces were analyzed by X-ray photoelectron spectroscopy (XPS) (PHI Quantera SXM) analysis. The soluble arsenic ions were measured by atomic fluorescence spectrophotometry (AFS) (AFS – 2202E, Beijing Haiguang Instrument Co.). The pH values of the soak solutions with different concentrations of biochar were continuously monitored by a pH meter (PHSJ-4A). The details of the characterization are shown in Text S1.

2.4. Electrochemical tests

Electrochemical experiments were performed on an electrochemical workstation (PARSTAT 2273) using a three-electrode system. The arsenopyrite electrode, saturated calomel electrode and platinum electrode acted as the working electrode, reference electrode and auxiliary electrode, respectively. AMD without/with biochar prepared as the above acted as electrolyte. The three electrodes were immersed in about 30 mL solution to adjust different experimental temperatures via a

constant temperature incubator. Temperature is one of the important factors that affect arsenopyrite weathering. In this work, four typical ambient temperatures 5 °C, 15 °C, 25 °C and 35 °C were selected as experimental temperatures. All the potentials reported in this work are relative to the SCE (0.245 V versus standard hydrogen electrode at 25 °C) unless otherwise stated.

Cyclic voltammetry (CV), polarization curves and electrochemical impedance spectroscopy (EIS) were adopted for electrochemical measurements. CV experiments were carried out at a scanning rate of 20 mV·s^{-1}, from the open circle potential (OCP) to 750 mV, then reverse scanned to $-$750 mV, and finally returned to OCP as the final potential. In this work, two cycles were carried out, and only the second cycle was reported. Polarization curve measurements were carried out from -0.25 V to $+0.25$ V (vs OCP) at a scanning rate of 10.0 mV·s^{-1}. EIS tests were performed at the OCP with frequencies ranging from 10^{-3} to 10^{4} Hz with an amplitude of 10.0 mV. The experiments were carried out in triplicate to ensure reproducibility, and the average results were reported in this study.

3. Results and discussion

3.1. Dissolution experiments immersion experiments

After erosion for 2 months, the AFS measurements (Table 1) show that the element As of arsenopyrite transformed to As(III) and As(V) ions, and the concentration of As(V) was dominant. The presence of biochar dramatically removed As(III) and As(V) ions, and the removal efficiency reached 90.39 % and 95.38 %, respectively, when there was 1.2 g·L^{-1} biochar. Acidity as the main indicator of AMD was also investigated.

Fig. 1 shows the variation in pH with time for the weathering of arsenopyrite in AMD in the presence of different concentrations of biochar at 25 °C. In the first 10 min, all the pH values of AMD dramatically decreased and gradually gently decreased until approximately 2 days. Afterwards, to that AMD without biochar, the pH value first gradually increased, then gradually decreased, and reached a relatively flat pH value of 2.75 at approximately 55–65 days. To those AMD with biochar, all the pH values gradually increased until reaching flat pH values of approximately 3.5–4.0, and a larger concentration of biochar corresponded to a higher pH value. All of the results revealed that biochar increased the pH of AMD, and the cause was biochar inhibit arsenopyrite oxidization, besides biochar presents alkaline (pH 9.7) itself (Buss et al., 2018; Pandit et al., 2018). The detailed explains will be revealed in the electrochemical analysis section.

3.2. Surface morphology, element composition and phase analysis

The surface morphologies of pristine and eroded arsenopyrite were observed by SEM (Fig. 2).

The surface of arsenopyrite before erosion was smooth and clean. After weathering for 2 months, all of them showed the presence of micro-particles with sizes between 200 nm and 1000 nm, and the degree of corrosion gradually decreased with increasing biochar concentration. The EDS results show that the corrosion products were comprised of Fe, As, S, O, and C when electrolyte had biochar (Table 2). Furthermore,

Table 1
Concentration of arsenic ions in AMD solutions with different concentrations of biochar.

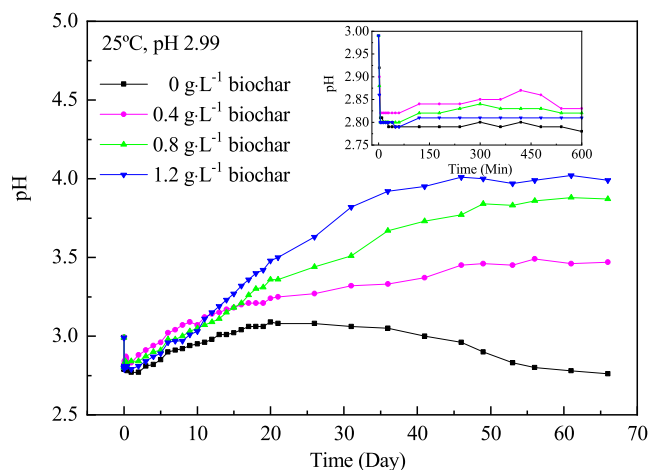| $c_{biochar}$ (g·L^{-1})	$c_{As(III)}$ (µg·L^{-1})	As$_{(III)}$ removal efficiency (%)	$c_{As(V)}$ (µg·L^{-1})	As$_{(V)}$ removal efficiency (%)
0	707.25	–	1303.80	–
0.4	456.25	35.49	740.55	43.20
0.8	92.45	86.93	161.40	87.62
1.2	67.95	90.39	60.30	95.38

Fig. 1. The variation of pH with time during leaching of arsenopyrite in AMD with different concentrations of biochar.

with increasing concentrations of biochar, there was a decrease in elemental content (At. %) for Fe, As, S and O, suggesting that biochar inhibits the oxidation of arsenopyrite. Fig. S3(a1-e1) and Table S5 display the XPS Fe 2p (3/2) spectra and corresponding fitting results of original and weathered arsenopyrite. The references for these XPS peaks are shown in Table S6. The results show that the composition of pristine arsenopyrite is 67.52 % at Fe(II) - AsS and 32.49 % at Fe(III) - AsS, meaning that the pristine arsenopyrite almost not be oxidized. After corrosion for two months, the content of Fe(II) increased from 18.00 % to 39.06 % and the content of Fe(III) decreased from 82.00 % to 60.94 % with biochar concentration increased to 1.2 g·L^{-1}. In addition, Fe(III) - O also decreased from 23.77 % to 15.4 %. All of the results confirmed the inhibition of biochar on arsenopyrite oxidation.

Fig. S3(a2-e2, a3-e3) and Tables S7- S8 show the XPS As 3d$_{(5/2)}$ and S 2p$_{(3/2)}$ spetra and the corresponding fitting results of arsenopyrite and weathered arsenopyrite. For pristine arsenopyrite, in terms of the arsenic species, As(-I)-S accounts for the highest content, reaching 70.20 %.

In terms of the sulfur species, S^{2-} and (AsS)$^{2-}$ account for the main contents, which are 27.05 % and 48.65 %, respectively. After weathering for 2 months, the content of As(-I)-S in the eroded arsenopyrite was significantly lower than that in the pristine arsenopyrite, while the content of As(V)-O was higher than that in the pristine mineral. With increasing biochar concentration in the solution, there was a gradual increase in the content of As(-I)-S, while the content of high-valence As (V)-O decreased significantly. Also, an increase in the total content of low oxidation state arsenic (As(-I)-S, As(0), and As(I)-O) and a decrease in the high oxidation state arsenic (As(III)-O and As(V)-O) total content were indicated. Moreover, the content of (AsS)$^{2-}$ increased distinctly with increasing biochar concentration, from 36.73 % to 47.98 %, while the content of SO$_4^{2-}$ decreased from 14.33 % to 6.38 %. The fitting results confirmed that the presence of biochar inhibited the oxidation of arsenopyrite.

Fig. 3(a) shows the Raman spectra of the biochar and the pristine and eroded arsenopyrite specimens. Pristine arsenopyrite showed four peaks at 244, 274, 388 and 407 cm^{-1}, which are spectral characteristic peaks of arsenopyrite (Lara et al., 2016; McGuire et al., 2001; Mernagh and Trudu, 1993). For biochar, two main overlapping bands at approximately 1350–1370 cm^{-1} and 1580–1600 cm^{-1} corresponded to the in-plane vibrations of sp^2-bonded carbon structures with structural defects (D band) and to the in-plane vibrations of the sp^2-bonded graphitic carbon structures (G band), respectively (Zhang et al., 2018).

After weathering for 2 months, all the eroded arsenopyrite acquired four additional peaks at 155, 220, 470 and 845 cm^{-1}. The three peaks at 155, 220, and 470 cm^{-1} correspond to elemental sulfur S (Murciego
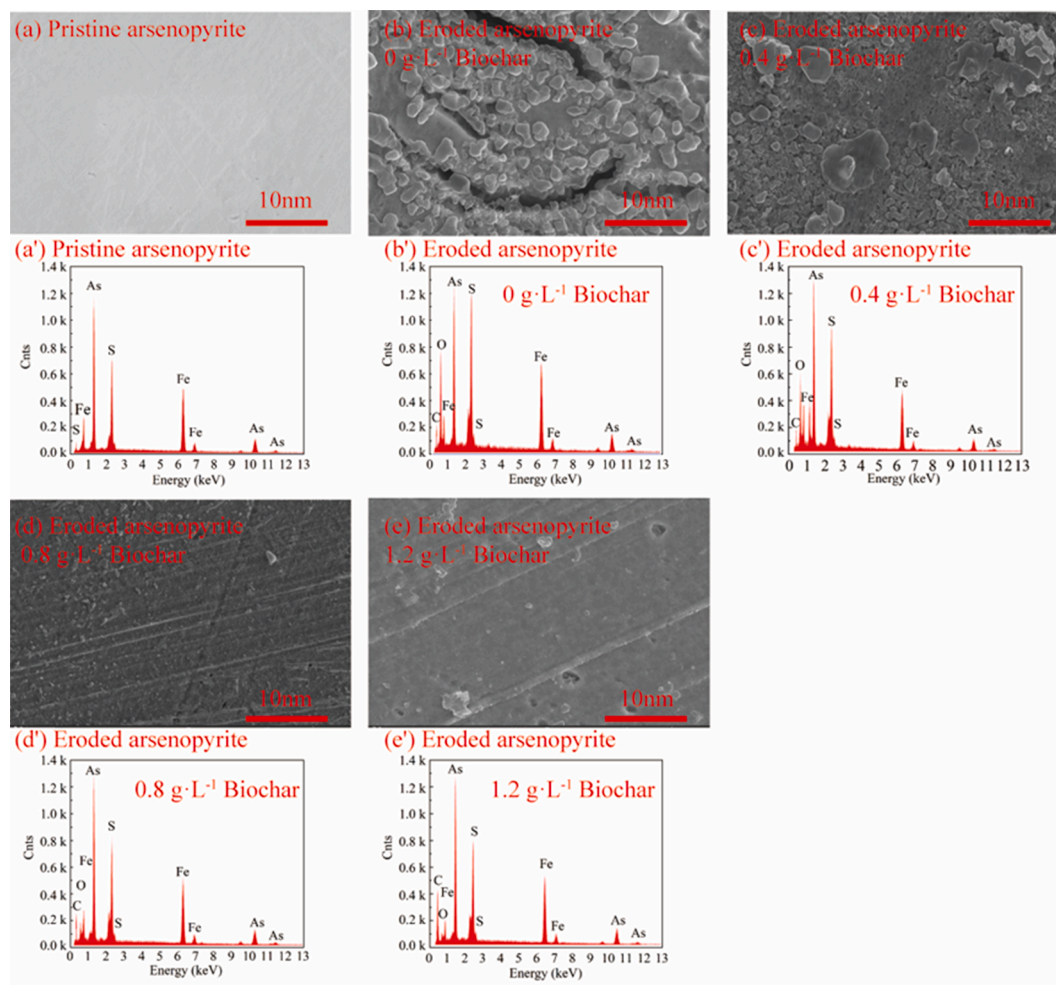
Fig. 2. SEM and EDS images of the pristine arsenopyrite (a, a') and eroded arsenopyrite (b-e, b'-e') in AMD with different concentrations of biochar for 2 months. Condition: 25 °C, pH 2.99.

Table 2
EDX for the pristine and the eroded arsenopyrite in pH 2.99 AMD with different concentration of biochar (25 °C, pH 2.99).

Specimen	Element content (At. %)				
	Fe	As	S	O	C
Pristine arsenopyrite	33.6	32.3	34.1	–	–
Eroded arsenopyrite, 0 g·L^{-1} biochar	25.4	24.0	24.0	26.7	–
Eroded arsenopyrite, 0.4 g·L^{-1} biochar	15.4	13.6	18.3	11.6	41.2
Eroded arsenopyrite, 0.8 g·L^{-1} biochar	14.0	13.0	18.0	8.7	46.3
Eroded arsenopyrite, 1.2 g·L^{-1} biochar	12.0	12.1	13.2	4.3	58.5

et al., 2019), while 845 cm^{-1} is derived from the asymmetric stretching mode of ferric arsenate FeAsO$_4$ (Murciego et al., 2011). Meanwhile, when the AMD solution contained different concentrations of biochar, peaks at 1350–1370 cm^{-1} and 1580–1600 cm^{-1} also appeared, suggesting the adsorption of biochar on the arsenopyrite surface. Fig. 3(b) shows the FTIR spectra of biochar, pristine and eroded arsenopyrite in AMD. The biochar exhibited five absorption peaks, the C—H bond vibrations in aromatic compounds at 750, 815 and 875 cm^{-1} (Niazi et al., 2018), the –OH of phenols and/or carboxyl peaks at 1035 and 1380 cm^{-1} (Niemeyer et al., 1992; Amir et al., 2010), and the carboxyl peak at 1600 cm^{-1} (COO–, C═O stretching and possibly aromatic C═C skeletal vibrations) (Amir et al., 2010). In the pristine arsenopyrite FTIR spectra, the peak at 1637 cm^{-1} is a characteristic peak of arsenopyrite (Wang et al., 2021). After weathering in AMD for 2 months, there was no new peak except at 815 cm^{-1} for the C—H bond vibration in aromatic compounds from biochar. Fig. 3(c) shows the spectra of 40 mg biochar immersed in 20 mL solution with pH 5.0 containing 0.0048 mol·L^{-1} As (V) and/or 0.0048 mol·L^{-1} Fe(III) ions. When the immersion solution contained Fe(III) ions, two new peaks appeared: one peak was attributed to Fe-O at 600 cm^{-1} (Zhang et al., 2021), and the other peak was the –OH of phenols and/or carboxyl peak at 1035 cm^{-1} shifted to 1130 cm^{-1}, meaning that the –OH groups of biochar complexed with Fe(III) (Sharma et al., 2010). When the immersion solution contained As(V) ions, no FTIR peak of arsenic complexing with biochar was detected, probably because its surface was negatively charged (the zeta potentials of AMD with 0.4, 0.8 and 1.2 g·L^{-1} biochar were −2.48, −4.30 and −5.80 mV, respectively) and thus had limited ability to adsorb As(V) ions (Hu et al., 2015). When the immersion solution contained Fe(III) and As(V) ions, a new peak at 827 cm^{-1} appeared for the As(V)/Fe/ biochar system and was attributed to an asymmetric ν_{as}(As-O-Fe) vibration from a compound peak of scorodite/ferric arsenate (Tabelin et al., 2019; Zhang et al., 2021). In addition, the COO$^-$ peak at 1600 cm^{-1} shifted to 1615 cm^{-1} in the Fe-biochar system, indicating As(V) binding with Fe-biochar(–OH) and forming a ternary complex As(V)-Fe-biochar through metal bridge mechanisms (Sharma et al., 2010). In this work, when arsenopyrite weathered in AMD, peaks from biochar complexations were not observed, perhaps due to the amount of arsenic and iron ions from arsenopyrite weathering being too small to detect.
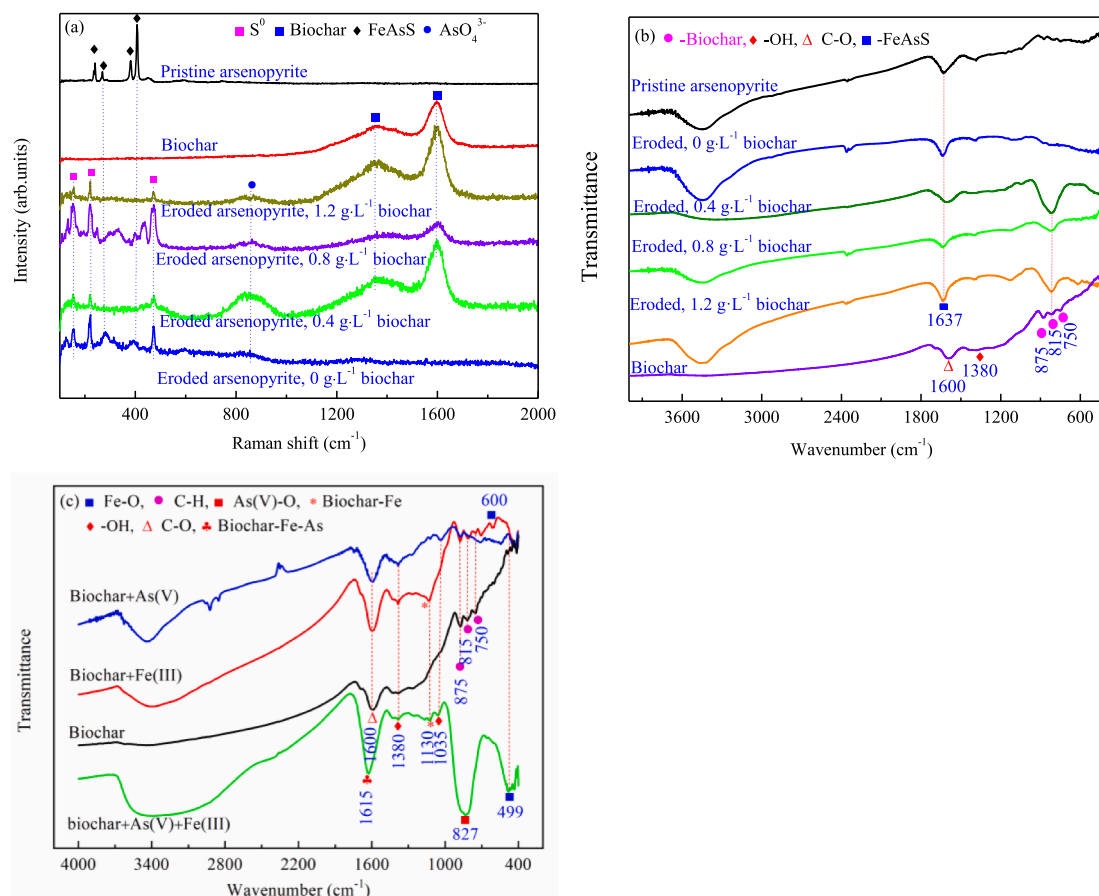
Fig. 3. Raman (a), FTIR (b) spectra of pristine biochar, pristine and eroded arsenopyrite, and FTIR (c) spectra of Biochar dropped with As(V) and/or Fe(III).
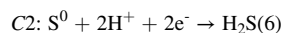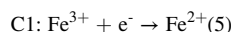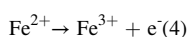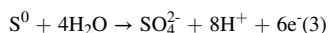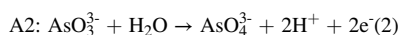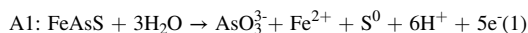
3.3. Electrochemical analysis

3.3.1. Cyclic voltammetry study: Arsenic transformation

Cyclic voltammetry provides rapid information on thermodynamic redox processes, on the kinetics of heterogeneous electron-transfer reactions, and on coupled chemical reactions or adsorption processes (Gosser, 1993), and hence is widely used to acquire qualitative and quantitative information about electrochemical reactions.

Fig. S4 shows the cyclic voltammetry curves of arsenopyrite in AMD at different biochar concentrations (a), different temperatures (b) and different acidities (c). All these curves had two anodic peaks (A1, A2) and two cathodic peaks (C1 and *C*2), indicating a similar oxidation–reduction mechanism of arsenopyrite under these conditions. During the anodic scanning process, the appearance of the first anodic peak A1 at approximately 200 mV was due to the oxidation of arsenopyrite and transformation to AsO_3^{3-}, Fe^{2+} and S^0 (Lázaro et al., 1997).

With a further increase in potential towards the positive direction, another anodic peak A2 appeared at 600–700 mV, which was attributed to further oxidation of AsO_3^{3-}, Fe^{2+} and S^0 to AsO_4^{3-}, Fe^{3+} and SO_4^{2-}, respectively (Zhang et al., 2020b). During reverse scanning in the negative direction, the first cathodic peak C1 appeared at approximately 400 mV, corresponding to the reduction of Fe^{3+}, while the reduction of S^0 generated the second cathodic peak *C*2 at approximately −650 mV (Tu et al., 2017).

A1: $FeAsS + 3H_2O \rightarrow AsO_3^{3-} + Fe^{2+} + S^0 + 6H^+ + 5e^-$ (1)

A2: $AsO_3^{3-} + H_2O \rightarrow AsO_4^{3-} + 2H^+ + 2e^-$ (2)

$S^0 + 4H_2O \rightarrow SO_4^{2-} + 8H^+ + 6e^-$ (3)

$Fe^{2+} \rightarrow Fe^{3+} + e^-$ (4)

C1: $Fe^{3+} + e^- \rightarrow Fe^{2+}$ (5)

*C*2: $S^0 + 2H^+ + 2e^- \rightarrow H_2S$ (6)

3.3.2. Polarization curve study: Arsenic releases kinetic and thermodynamic parameters

Under the natural conditions, the arsenopyrite weathering tendency and arsenic release rate are of great concern. The polarization curve provides information on the corrosion likelihood and rate; in this respect, it is a very effective means to answer the concerned questions (Mansfeld, 2005). In this work, four temperatures (5, 15, 25 and 35 °C), four pH values (pH 1.99, 2.99, 3.99 and 4.99) and four different concentrations of biochar (0, 0.4, 0.8, 1.2 g·L⁻¹) were used to investigate their effects on the weathering of arsenopyrite.

Fig. S5 shows the polarization curves of arsenopyrite in AMD with different biochar concentrations at natural temperatures of 5 °C, 15 °C, 25 °C and 35 °C. All these curves had similar shapes, indicating similar oxidation mechanisms. Furthermore, the curves shift to the lower left with increasing biochar concentration, meaning that a higher concentration of biochar results in a more negative corrosion potential (E_{corr}) and larger corrosion current density (i_{corr}). Here, the values of E_{corr} and i_{corr} can be obtained employing the method of Tafel extrapolation (Bard and Faulkner, 2001). Furthermore, the weathering rate of arsenopyrite can be further achieved by Faraday's equation using the corrosion current density i_{corr}, namely, $\nu = \frac{M i_{corr}}{nF}$, where ν is the weathering rate, mg·cm⁻²·h⁻¹; M is the atomic weight, g·mol⁻¹; n is the valence state of the element; and F is the Faraday constant, 96,485 C·mol⁻¹. The detailed weathering parameters of arsenopyrite in AMD in the presence of

different concentrations of biochar are listed in Table 3.

In real environment, the parameter i_{corr} reflects the weathering rate of arsenopyrite, that is, a larger i_{corr} meaning faster weathering rate. The parameter E_{corr} is related to the weathering possibility, i.e., a more positive value of E_{corr} meaning arsenopyrite is difficult to erode. Taking 25 °C as an example, increasing the biochar concentration from 0 to 0.4 g·L^{-1} resulted in a shift in E_{corr} from 264.61 to 250.25 mV, ultimately reaching 228.45 mV when the biochar concentration was increased to 1.2 g·L^{-1}. Meanwhile, the corresponding value of $v_{As(III)}$ decreased from 1.46E to 3 to 8.74E-4 mg·cm^{-2}·h^{-1}, ultimately reaching 5.79E-4 mg·cm^{-2}·h^{-1}. The results indicated that biochar inhibited arsenopyrite weathering, and the higher the concentration of biochar was, the more inhibited the oxidative dissolution of arsenopyrite. The reason can be as follows: in the AMD media, arsenopyrite acted as the anode, and reaction (1) took place. At the cathode, reduction of Fe^{3+} ions and dissolved O$_2$ would take place as per reaction (5) and reaction (7).

In comparison with the concentration of Fe^{3+} ions in the AMD, the concentration of dissolved O$_2$ is smaller (8.0–8.5 mg·L^{-1} at room temperature), and Fe^{3+} ions also have stronger oxidizing capability than O$_2$. Hence, the reduction reaction of Fe^{3+} ions is dominant. With the addition of biochar, some Fe^{3+} ions are absorbed, complexed to Fe-OH (biochar) and As(V)-O-Fe, as previously mentioned, and even reduced to Fe^{2+} by biochar (Chen et al., 2016; Kappler et al., 2014; Xu et al., 2019). Fig. S6 and Table S9 show the various absorption and reduction efficiencies of biochar to Fe^{3+} ions. The results confirmed the strong sorption and reduced effect of Fe^{3+} ions caused by biochar; by comparison, its absorption efficiency was dominant. The higher the concentration of biochar, the larger the absorption and reduction efficiencies. Obviously, the decreasing concentration of Fe^{3+} ions is disadvantageous for its reduction and further inhibits the oxidation of arsenopyrite.

Thus far, the pH variation of arsenopyrite AMD with different concentrations of biochar shown in Fig. 1 can be explained. That is, during this initial stage, arsenopyrite was strongly oxidized in the presence of Fe^{3+} ions, released a large amount of H$^+$ as reaction (1) and resulted in a dramatic decrease in the pH value. Due to oxygen has a large overpotential and oxygen be reduced (reaction (7)) is a several steps 4-electron reaction. When Fe^{3+} ions decreased to a very small concentration, oxygen would participate in the cathode reaction and gradually consumed H$^+$ ions; meanwhile, the increase in the S^0 and FeAsO$_4$ passivation films caused the oxidation of arsenopyrite to become increasingly difficult. All these causes resulted in the concentration of H$^+$ ions decreasing, i.e., the pH value increasing. Finally, with the termination of the weathering process of arsenopyrite, the pH value of

AMD would reach relatively flat pH values, the higher concentration of biochar caused the larger pH value, for higher adsorption capacity to H$^+$ ions and higher adsorption/reduction capacities to Fe^{3+} ions as the above mentioned with biochar concentration increasing. Interestingly, to that AMD without biochar, its pH value reached a maximum and gradually decreased before reaching a relatively flat pH value. The cause was as follows: when there was 1 mol electron transfer, arsenopyrite weathering would release 1.2 mol H$^+$ ions (reaction (1)) while consuming only 1.0 mol H$^+$ ions (reaction (7)), i.e., more H$^+$ ions accumulated in the AMD.

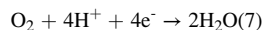$$O_2 + 4H^+ + 4e^- \rightarrow 2H_2O (7)$$

Fig. S7 and Table S10 show the polarization curve and Tafel parameters of arsenopyrite in AMD at different temperatures, and the results showed that higher temperatures promoted arsenopyrite weathering. The reason is the greater transformation of internal energy to electrochemical energy at higher temperatures. Fig. S8 and Table S11 are the polarization curve and Tafel parameters of arsenopyrite in AMD at different acidities, and the results suggest a smaller weathering tendency and a faster weathering rate at high acidity. The reason is that higher acidity promotes cathodic reduction of O$_2$ as the reaction (8). To describe the inhibition effect of biochar more intuitively, "inhibiting efficiency (η)" is defined as $\eta = (i_{corr} - i_{corr}^0)/i_{corr}^0$, which is often used in material science (Solmaz et al., 2008). Here, i_{corr}^0 and i_{corr} are the corrosion current density before and after the change of condition, respectively. The inhibiting efficiency η of biochar concentration, temperature, and AMD acidity are listed in Table 3, Table S10 and Table S11. Fig. S9 shows the As(III) inhibiting efficiency of biochar at different concentrations and temperatures. The results show that a larger concentration of biochar inhibits the weathering of arsenopyrite at the same environmental temperature; however, with a continuous increase in biochar concentration, the amplitude of the inhibiting efficiency will decrease. For the same concentration of biochar, the promotion efficiency increased with increasing temperature, and with a continuous increase in temperature, the amplitude of the promotion efficiency increased. The above results show that there is an optimal consumption of biochar for inhibiting arsenic ion release from arsenopyrite weathering, and this will be discussed in the next section.

Arsenic ion release rate is a very important dynamic parameter for investigating the environmental effect of arsenopyrite weathering. According to Table 3, Table S10 and Table S11, the relationships of the As(III) release rate ($v_{As(III)}$) from arsenopyrite weathering and the concentration (c) of biochar, environmental temperature (T), and AMD acidity (pH) are listed in Fig. 4 (a-c). The results show that (1) at experimental temperatures of 5 °C, 15 °C, 25 °C or 35 °C, the As(III) release rate ($v_{As(III)}$) and the concentration (c) of biochar had a negative linear correlation (Fig. 4a). Based on these relationships, it can be deduced that the optimal consumption of biochar for the weathering rate tends to zero. Taking 25 °C as an example, the optimal consumption of biochar for AMD from the Xingwen mine was 2.79 g·L^{-1}. The As(III) release rate ($v_{As(III)}$) and environmental temperature (T) had a negative linear correlation (Fig. 4b), meaning that a higher temperature promotes arsenic ion release. For the fitted linear curve of the As(III) release rate ($v_{As(III)}$) and the acidity of AMD (Fig. 4c), the R^2 was 0.8399, suggesting a nonlinear relationship. The reason is Fe^{3+} ions in AMD, like H$^+$ ions, also participated in the cathode reaction. Especially, during the electrochemical processes, the reduction of Fe^{3+} ions was dominant for its large concentration.

The activation energy (E_a), activation enthalpy (ΔH^*) and activation entropy (ΔS^*) are three important parameters that reflect the thermodynamic stability of arsenopyrite weathering in AMD. Based on the Arrhenius equation, activation energies (E_a) can be calculated by linear regression between ln$v$ and $1/T$ as $\ln v = (\frac{-E_a}{RT}) + \ln A$ (Arrhenius, 1889). where v is the reaction rate constant, mg·cm^{-2}·h^{-1}; E_a is the activation energy, J·mol^{-1}; R is the gas constant, 8.314 J·mol^{-1}·K^{-1}, T is the

Table 3
Tafel parameters of arsenopyrite in AMD at different concentrations of biochar, and the As(III) releases rate and biochar inhibiting efficiency.

Temperature (°C)	$c_{Biochar}$ (g·L^{-1})	E_{corr} (mV)	i_{corr} (μA·cm^{-2})	$v_{As(III)}$ (mg·cm^{-2}·h^{-1})	η
5	0	303.46	0.651	6.07E-4	–
	0.4	270.98	0.438	4.08E-4	32.78
	0.8	247.85	0.375	3.49E-4	42.50
	1.2	239.35	0.343	3.20E-4	47.28
15	0	282.35	1.183	1.10E-3	–
	0.4	252.88	0.751	7.00E-4	36.36
	0.8	243.28	0.621	5.79E-4	47.36
	1.2	234.52	0.536	4.99E-4	54.64
25	0	264.61	1.568	1.46E-3	–
	0.4	250.25	0.938	8.74E-4	40.14
	0.8	239.68	0.794	7.40E-4	49.32
	1.2	228.45	0.621	5.79E-4	60.34
35	0	253.89	2.308	2.15E-3	–
	0.4	233.78	1.221	1.14E-3	46.98
	0.8	223.35	0.946	8.81E-4	59.02
	1.2	209.12	0.824	7.68E-4	64.28

E_{corr}: corrosion potential; i_{corr}: corrosion current density; $v_{As(III)}$: release rate of As(III); η: inhibiting efficiency.
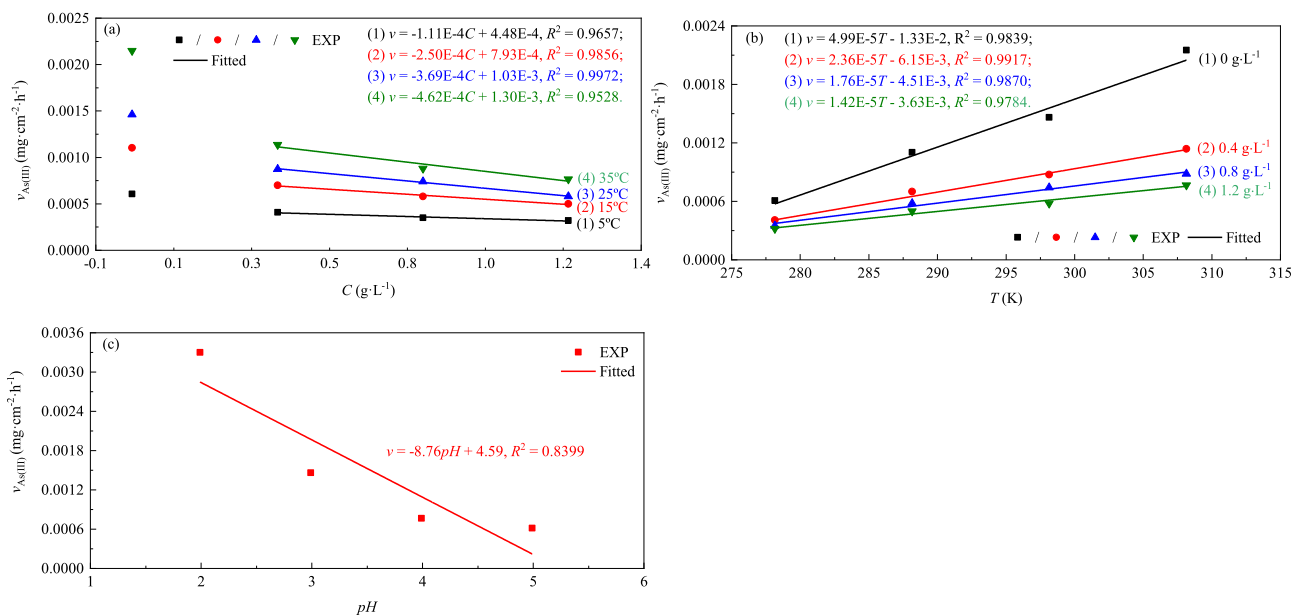
Fig. 4. Variation in corrosion rate of arsenopyrite with biochar concentration (a), temperature (b) and acidity (c).

absolute temperature and A is the pre-exponential factor. According to the results shown in Table 3, the activation energies (E_a) of arsenopyrite weathering in AMD at different concentrations of biochar were calculated by using linear regression between ln$v$ and $1/T$, and the results are listed in Table 4.

The results indicate a decreasing trend of activation energy when the concentration of biochar was increased. Here, the activation energy (E_a) of arsenopyrite weathering in AMD absence of biochar was 29.15 KJ·mol^{-1}, corresponding to the result of arsenopyrite oxidation in dilute acid at an apparent activation energy of 33 kJ·mol^{-1} (Fernandez et al., 1996). Especially, all these activation energies were higher than 20 kJ·mol^{-1} when the biochar concentration in AMD no>0.8 g·L^{-1}. According to reaction kinetic theory, the rate of oxidation of arsenopyrite is controlled by surface interaction (Lasaga, 1998). When the biochar concentration in AMD was 1.2 g·L^{-1}, the E_a decreased 19.85 kJ·mol^{-1} (<20 kJ·mol^{-1}), meaning that the rate of oxidation of arsenopyrite is controlled by mass transport of dissolve species (diffusion control). The shift of rate-determining step of arsenopyrite oxidation further confirmed that high concentration of biochar can effectively "remove" (adsorbed, oxidized and complexed, etc.) the ions involved in the anode reaction.

According to transition state theory, the activation enthalpy (ΔH^*) and activation entropy (ΔS^*) of arsenopyrite weathering can be calculated from the linear regression between ln(v/T) and $1/T$ (Fig. S10) as $In\left(\frac{v}{T}\right) = \left(In\left(\frac{R}{N_A h}\right) + \left(\frac{\Delta S^*}{R}\right)\right) - \frac{\Delta H^*}{RT}$ (Hegazy et al., 2012). where v is the corrosion rate, mg·cm^{-2}·h^{-1}; T is the absolute temperature, K; N_A is Avogadro's number, 6.02E23 mol^{-1}; h is Planck's constant, 6.626E-34 J·S; R is the universal gas constant, 8.314 J·mol^{-1}·K^{-1}. Data in Table 4 represent the values of ΔH^* and ΔS^*. The values of $\Delta H^* > 0$ for all the conditions indicate the endothermic nature of the weathering process of arsenopyrite and reflect that high temperature is conducive to the

weathering of arsenopyrite (Refaey et al., 2004). Moreover, the value ΔH^* decreased with increasing biochar concentration, signifying that more biochar is beneficial for the adsorption and Fe^{3+} ion reduction process. $\Delta S^* < 0$ suggested that the activation process was associated rather than dissociated in the rate-determining step; that is, disorder was reduced from the reactant to the transition state/activated complex (Benabdellah et al., 2006).

3.3.3. Electrochemical impedance spectroscopy (EIS) study: arsenopyrite-AMD surface passivation mechanism

As an important electrochemical technique based on the interfacial reaction at the electrode surface, EIS technique has been widely used in mineral corrosion studies to obtain information about the electrochemical reactions that occur on the surface of minerals, such as the internal resistance and coating layers. Fig. 5 shows the Nyquist (a-c) and Bode (a'-c') plots for arsenopyrite weathering in AMD at different biochar concentrations, temperatures, and acidities. All these Nyquist plots showed two capacitor loops. The capacitance loop at high frequency corresponds to the pseudo-capacitance and resistance of the surface layer, while at low frequency, it is attributed to the double-layer capacitance and charge transfer resistance between the solution/mineral interfaces. Electrochemical equivalent circuit (EEC) represents an approach to describe the electrochemical processes that occur at the electrode and/or electrolyte interface. Macdonald (1985) pointed out that any model derived from them is only tentative. For this reason, the selected EEC must be effectively explaining the electrochemical processes, and has the best fit results. The EEC shown in Fig. 5 (d) was used to simulate the electrochemical process.

Here, R_s is the ohmic resistance of the solution, and R_f is the passivation film resistance. R_t is the charge transfer resistance at the double layer. CPE is a constant phase element used to substitute capacitance for loops deviating from an ideal semicircle, where CPE_f represents capacitance of the passivation film and CPE_{dl} represents capacitance of the double layer. The model parameters for arsenopyrite weathering in AMD under different conditions are shown in Table 5. When arsenopyrite was weathered in AMD with different concentrations of biochar, the results showed that transfer resistance R_t increased while passivation film resistance R_f decreased with increasing concentration of biochar, besides, the values of R_t were larger than that of R_f, which confirmed that higher concentration of biochar inhibited the oxidation of arsenopyrite for more Fe^{3+} ions were absorbed or reduced by biochar.

Table 4
Activation parameters for arsenopyrite in pH 2.99 AMD with different concentrations of biochar.

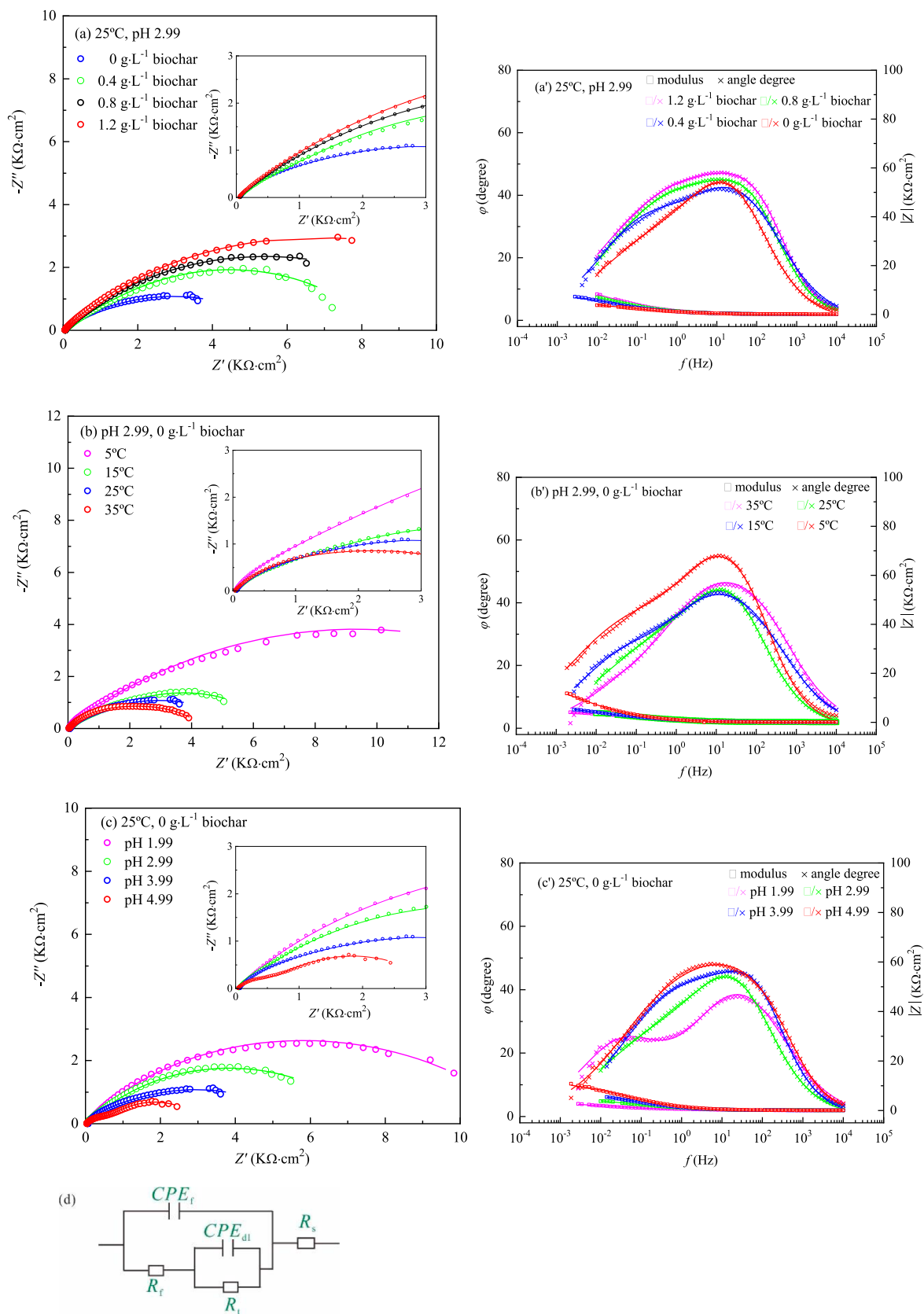| $c_{Biochar}$ (g·L^{-1})	E_a (KJ·mol^{-1})	ΔH_{ads}^* (KJ·mol^{-1})	ΔS_{ads}^* (J·mol^{-1}·K^{-1})
0	29.15	26.72	−209.39
0.4	23.62	21.19	−232.43
0.8	21.68	19.25	−237.29
1.2	19.85	17.42	−244.81

Fig. 5. Nyquist (a, b, c) and Bode plots (a′, b′, c′) for arsenopyrite in AMD at different concentrations of biochar (a, a′), temperature (b, b′), acidities (c, c′), and equivalent circuit (d), where ○, □ and × represent the experimental values and — represents simulated values.

Table 5
Equivalent circuit model parameters for arsenopyrite in AMD at different conditions.

$c_{Biochar}$ (g·L^{-1})	Temperature (°C)	pH	CPE_f, Y_0 (S·cm^{-2}·s^{-n})	n	R_f (Ω·cm^2)	CPE_{dl}, Y_0 (S·cm^{-2}·s^{-n})	n	R_t (Ω·cm^2)	χ^2
0	25	2.99	9.545E-5	0.725	4.107E3	1.356E-3	0.554	3.846E3	6.994E-5
0.4	25	2.99	1.627E-4	0.641	1.360E3	3.329E-4	0.538	7.133E3	1.627E-4
0.8	25	2.99	8.056E-5	0.748	4.443E2	2.423E-4	0.484	1.050E4	5.085E-5
1.2	25	2.99	6.312E-5	0.779	3.047E2	2.233E-4	0.481	1.361E4	5.271E-5
0	5	2.99	1.553E-4	0.734	1.237E3	5.422E-4	0.478	1.244E4	1.570E-4
0	15	2.99	2.446E-4	0.598	2.237E3	8.774E-4	0.599	4.096E3	3.211E-4
0	25	2.99	9.545E-5	0.725	4.107E3	1.356E-3	0.554	3.846E3	6.994E-5
0	35	2.99	1.893E-4	0.631	2.194E3	9.654E-4	0.496	2.253E3	1.893E-4
0	25	4.99	4.792E-5	0.786	1.365E2	1.754E-4	0.492	1.175E4	4.068E-4
0	25	3.99	6.434E-5	0.780	2.612E2	2.214E-4	0.506	9.279E3	5.567E-5
0	25	2.99	9.545E-5	0.725	4.107E3	1.356E-3	0.554	3.846E3	6.994E-5
0	25	1.99	2.680E-5	0.633	6.763E3	2.111E-3	0.595	2.496E3	6.419E-4

R_f: passive film resistance; R_t: charge transfer resistance; n: dimensionless number;
CPE_{dl}: constant phase element of double layer; CPE_f: constant phase element of passive film.

For arsenopyrite weathering in AMD at different temperatures, the results showed that with increasing temperature, there was a decrease in the value of R_t at the double layer, while the value of R_f was increased. The reason was that higher temperature promotes ion transfer at the double layer, which was advantageous for the oxidation of arsenopyrite, and simultaneously, more S^0 and $FeAsO_4$ would be produced, which will cover the surface of arsenopyrite. It is interesting to note that the value of R_f at 35 °C was larger than that at 25 °C, which is due to the loosening of the passivation film as a consequence of enhanced penetration of Cl$^-$ ions with increased temperature. When arsenopyrite was weathered in AMD at different acidities, the results showed that the value of R_t in the double layer and R_f decreased and increased, respectively, with increasing acidity. The results confirmed that higher acidity (more H$^+$ ions) promotes charge transfer at the double layer, which was beneficial for the oxidation of arsenopyrite and thus more S^0 and $FeAsO_4$ covering the surface of arsenopyrite.

3.4. The weathering mechanism of arsenopyrite and biochar inhibition mechanism

Combining the electrochemical experiments and surface analysis results, the weathering mechanism of arsenopyrite in AMD with/without biochar is summarized in Fig. 6.

Arsenopyrite weathering takes place via the following steps: FeAsS acts as an anode, is oxidized to low-valence Fe^{2+}, AsO_3^{3-} and S^0, and releases H$^+$ ions under the action of water molecules, which aggravates acid pollution. Fe^{2+} and AsO_3^{3-} are further oxidized to high-valence Fe^{3+} and AsO_3^{3-}, and S^0 transforms to SO_4^{2-} via the intermediate product of SO_3^{2-}. Fe^{3+} and O_2 in AMD act as oxidizing agents and are reduced at the cathode. The presence of biochar adsorbs and reduces the stronger

oxidizing agent Fe^{3+} and thus inhibits the further weathering of arsenopyrite. Meanwhile, biochar can also complex As(V) to biochar-Fe-As (V) through metal bridges. Then, Fe^{3+} and AsO_3^{3-} combine to form $FeAsO_4$ due to its low solubility. $FeAsO_4$ and S^0 may form passivation films and inhibit arsenopyrite further weathering. Higher temperature or stronger acidity promotes arsenopyrite weathering without changing its oxidation mechanism.

4. Environmental implications

The results show that arsenopyrite is readily weathered under AMD conditions, resulting in the release of arsenic and H$^+$ ions, thus prompting the spread of heavy metals to the surrounding environment. Higher acidity promotes arsenopyrite weathering, suggesting that the accumulation of H$^+$ will further deteriorate the surrounding environment if not dealt with in time. With biochar present it can be observed that the biochar can adsorb Fe^{3+} ions, bind with Fe and As(V) to form Fe-biochar(–OH) and ternary complex As(V)-Fe-biochar, thus inhibiting arsenopyrite weathering and also reducing the toxicity of arsenic. Thus, biochar may be a potential material for AMD purification when there is arsenopyrite. In situ electrochemical techniques will be simple but effective means to determine the optimal amount of biochar according to real chemical composition, acidity of AMD and environmental temperature. It can be predicted that electrochemical technology will play an important role in the evaluation and treatment of AMD in complex geological environment.

5. Conclusions

In this work, the effects of biochar, temperature and acidity of AMD
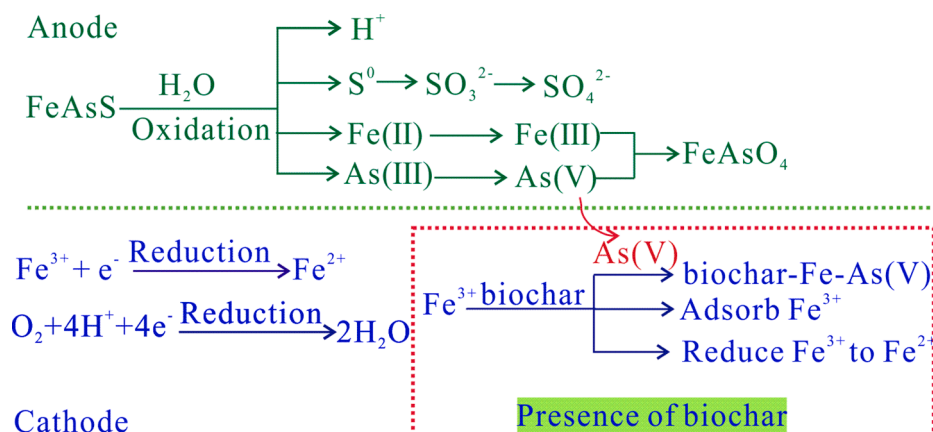

Fig. 6. Scheme of the inhibition mechanism of biochar for arsenopyrite weathering in AMD.

on As release from arsenopyrite were investigated using electrochemical and surface analysis techniques. In AMD, FeAsS is first oxidized to Fe^{2+}, AsO_3^{3-} and S^0 and releases H^+ ions under the action of water molecules, which aggravates acid pollution. Fe^{2+} and AsO_3^{3-} are further oxidized to Fe^{3+} and AsO_4^{3-}, and S^0 transforms to SO_4^{2-} via the intermediate product SO_3^{2-}. Higher temperature or higher acidity accelerates As release. The presence of biochar inhibits As release from arsenopyrite weathering without changing the weathering mechanism. The mechanisms responsible for the biochar inhibition As release and acidification are Fe^{3+} ions being adsorbed and oxidized to Fe^{2+} ions and As(V) being complexed to biochar-Fe-As(V) through metal bridge mechanisms. The positive activation enthalpy (ΔH^*) and negative activation entropy (ΔS^*) indicate the endothermic nature of the arsenopyrite weathering process, and the activated process was associated rather than dissociated in the rate determining step. These experiments provided a demonstration of a rapid and quantitative calculation for arsenic pollution using electrochemical techniques for arsenopyrite around mining sites. They also showed significance in assessing the risks of arsenopyrite in AMD and gave the optimal amount of biochar for AMD pollution control.

CRediT authorship contribution statement

Ling Cen: Investigation, Data curation, Visualization, Writing – original draft. **Hongguang Cheng:** Supervision, Funding acquisition, Methodology. **Qingyou Liu:** Conceptualization, Supervision, Funding acquisition, Writing – review & editing. **Shuai Wang:** Visualization, Formal analysis, Writing – original draft. **Xi Wang:** Data curation, Visualization.

Declaration of Competing Interest

The authors declare that they have no known competing financial interests or personal relationships that could have appeared to influence the work reported in this paper.

Data availability

Data will be made available on request.

Acknowledgements

Appendix A. Supplementary data

Supplementary data to this article can be found online at https://doi.org/10.1016/j.envint.2022.107558.

References

Ahmad, M., Rajapaksha, A.U., Lim, J.E., Zhang, M., Bolan, N., Mohan, D., Vithanage, M., Lee, S.S., Ok, Y.S., 2014. Biochar as a sorbent for contaminant management in soil and water: A review. Chemosphere 99, 19–33.

Amir, S., Jouraiphy, A., Meddich, A., Gharous, M., Winterton, P., Hafidi, M., 2010. Structural study of humic acids during composting of activated sludge-green waste: elemental analysis, FTIR and 13C NMR. J. Hazard. Mater. 177 (1–3), 524–529.

Arrhenius, S., 1889. Über die dissociationswärme und den einfluss der temperatur auf den dissociationsgrad der elektrolyte. Zeitschrift für Physikalische Chemie 4U (1).

Bard, A.J., Faulkner, L.R., 2001. Electrochemical methods: Fundamentals and applications, 2nd ed. Wiley and Sons, Hoboken.

Benabdellah, M., Aouniti, A., Dafali, A., Hammouti, B., Benkaddour, M., Yahyi, A., Ettouhami, A., 2006. Investigation of the inhibitive effect of triphenyltin 2-thiophene carboxylate on corrosion of steel in 2M H_3PO_4 solutions. Appl. Surf. Sci. 252 (23), 8341–8347.

Buckley, A.N., Walker, G.W., 1988. The surface composition of arsenopyrite exposed to oxidizing environments. Appl. Surf. Sci. 35 (2), 227–240.

Buss, W., Shepherd, J.G., Heal, K.V., Mašek, O., 2018. Spatial and temporal microscale pH change at the soil-biochar interface. Geoderma 331, 50–52.

Chen, Z., Wang, Y., Xia, D., Jiang, X., Fu, D., Shen, L., Wang, H., Li, Q.B., 2016. Enhanced bioreduction of iron and arsenic in sediment by biochar amendment influencing microbial community composition and dissolved organic matter content and composition. J. Hazard. Mater. 311, 20–29.

Cheng, H., Jones, D.L., Hill, P., Bastami, M.S., Tu, C.L., 2017. Influence of biochar produced from different pyrolysis temperature on nutrient retention and leaching. Arch. Agron. Soil Sci. 64 (6), 850–859.

Costa, M.C., Botelho do Rego, A.M., Abrantes, L.M., 2002. Characterization of a natural and an electro-oxidized arsenopyrite: a study on electrochemical and X-ray photoelectron spectroscopy. Int. J. Miner. Process. 65 (2), 83–108.

El-Naggar, A., Chang, S.X., Cai, Y., Lee, Y.H., Wang, J., Wang, S.-L., Ryu, C., Rinkleve, J., Sik Ok, Y., 2021. Mechanistic insights into the (im) mobilization of arsenic, cadmium, lead, and zinc in a multi-contaminated soil treated with different biochars. Environ. 156, 106638.

Fernandez, P.G., Linge, H.G., Wadsley, M.W., 1996. Oxidation of arsenopyrite (FeAsS) in acid Part I: Reactivity of arsenopyrite. J. Appl. Electrochem. 26 (6), 575–583.

Flora, S.J.S., 2015. Handbook of arsenic toxicology. Academic Press. 1–49.

Genc-Fuhrman, H., Bregnhoj, H., McConchie, D., 2005. Arsenate removal from water using sand-red mud columns. Water Res. 39 (13), 2944–2954.

Gosser, D.K., 1993. Cyclic voltammetry: simulation and analysis of reaction mechanisms. VCH New York, New York.

Hegazy, M.A., El-Tabei, A.S., Bedair, A.H., Sadeq, M.A., 2012. An investigation of three novel nonionic surfactants as corrosion inhibitor for carbon steel in 0.5M H_2SO_4. Corros. Sci. 54, 219–230.

Hong, J., Liu, L., Ning, Z., Liu, C., Qiu, G., 2021. Synergistic oxidation of dissolved As(III) and arsenopyrite in the presence of oxygen: Formation and function of reactive oxygen species. Water Res. 202, 117416.

Hu, X., Ding, Z., Zimmerman, A.R., Wang, S., Gao, B., 2015. Batch and column sorption of arsenic onto iron-impregnated biochar synthesized through hydrolysis. Water Res. 68, 206–216.

Huyen, D.T., Tabelin, C.B., Thuan, H.M., Dang, D.H., Truong, P.T., Vongphuthone, B., Kobayashi, M., Igarashi, T., 2019. The solid-phase partitioning of arsenic in unconsolidated sediments of the Mekong Delta, Vietnam and its modes of release under various conditions. Chemosphere 233, 512–523.

Kappler, A., Wuestner, M.L., Ruecker, A., Harter, J., Halama, M., Behrens, S., 2014. Biochar as an electron shuttle between bacteria and Fe(III) minerals. Environ. Sci. Technol. Lett. 1 (8), 339–344.

Lara, R.H., Velazquez, L.J., Vazquez-Arenas, J., Mallet, M., Dossot, M., Labastida, I., Sosa-Rodriguez, F.S., Espinosa-Cristobal, L.F., Escobedo-Bretado, M.A., Cruz, R., 2016. Arsenopyrite weathering under conditions of simulated calcareous soil. Environ. Sci. Pollut. Res. Int. 23 (4), 3681–3706.

Lasaga, A., 1998. Kinetic theory in the earth sciences. Princeton series in geochemistry. Princeton University Press, Princeton, New Jersey.

Lázaro, I., Cruz, R., González, I., Monroy, M., 1997. Electrochemical oxidation of arsenopyrite in acidic media. Int. J. Miner. Process. 50 (1–2), 63–75.

Lombard, M.A., Bryan, M.S., Jones, D.K., Bulka, C., Bradley, P.M., Backer, L.C., Focazio, M.J., Silverman, D.T., Toccalino, P., Argos, M., Gribble, M.O., Ayotte, J.D., 2021. Machine learning models of arsenic in private wells throughout the conterminous United States as a tool for exposure assessment in human health studies. Environ. Sci. Technol. 55 (8), 5012–5023.

Ma, Y., Qin, Y., Lin, C., 2014. The role of rainwater-borne hydrogen peroxide in the release of arsenic from arsenopyrite. Chemosphere 103, 349–353.

Macdonald, J.R., 1985. Generalizations of "universal dielectric response" and a general distribution-of-activation-energies model for dielectric and conducting systems. J. Appl. Phys. 58 (5), 1971–1978.

Mansfeld, F., 2005. Tafel slopes and corrosion rates obtained in the pre-Tafel region of polarization curves. Corros. Sci. 47 (12), 3178–3186.

McGuire, M.M., Edwards, K.J., Banfield, J.F., Hamers, R.J., 2001. Kinetics, surface chemistry, and structural evolution of microbially mediated sulfide mineral dissolution. Geochim. Cosmochim. Acta 65 (8), 1243–1258.

McKibben, M.A., Tallant, B.A., del Angel, J.K., 2008. Kinetics of inorganic arsenopyrite oxidation in acidic aqueous solutions. Appl. Geochem. 23 (2), 121–135.

Mernagh, T.P., Trudu, A.G., 1993. A laser Raman microprobe study of some geologically important sulphide minerals. Chem. Geol. 103 (1–4), 113–127.

Mikhlin, Y., Tomashevich, Y., 2005. Pristine and reacted surfaces of pyrrhotite and arsenopyrite as studied by X-ray absorption near-edge structure spectroscopy. Phys. Chem. Miner. 32 (1), 19–27.

Muñoz, J.A., Gomez, C., Ballester, A., Blazquez, M.L., Gonzalez, F., Figueroa, M., 1998. Electrochemical behaviour of chalcopyrite in the presence of silver and sulfolobus bacteria. J. Appl. Electrochem. 28 (1), 49–56.

Murciego, A., Alvarez-Ayuso, E., Pellitero, E., Rodriguez, M.A., Garcia-Sanchez, A., Tamayo, A., Rubio, J., Rubio, F., Rubin, J., 2011. Study of arsenopyrite weathering products in mine wastes from abandoned tungsten and tin exploitations. J. Hazard. Mater. 186 (1), 590–601.

Murciego, A., Álvarez-Ayuso, E., Aldana-Martínez, S.C., Sanz-Arranz, A., Medina-García, J., Rull-Pérez, F., Villar-Alonso, P., 2019. Characterization of secondary products in arsenopyrite-bearing mine wastes: influence of cementation on arsenic attenuation. J. Hazard. Mater. 373, 425–436.

Neil, C.W., Jun, Y.S., 2015. Fe^{3+} addition promotes arsenopyrite dissolution and iron (III) (Hydr)oxide formation and phase transformation. Environ. Sci. Technol. Lett. 3 (1), 30–35.

Niazi, N.K., Bibi, I., Shahid, M., Ok, Y.S., Burton, E.D., Wang, H., Shaheen, S.M., Rinkleve, J., Luttge, A., 2018. Arsenic removal by perilla leaf biochar in aqueous solutions and groundwater: An integrated spectroscopic and microscopic examination. Environ. Pollut. 232, 31–41.

Niemeyer, J., Chen, Y., Bollag, J.M., 1992. Characterization of humic acids, composts, and peat by diffuse reflectance fourier-transform infrared-spectroscopy. Soil Sci. Soc. Am. J. 56 (1), 135–140.

Pandit, N.R., Mulder, J., Hale, S.E., Martinsen, V., Schmidt, H.P., Cornelissen, G., 2018. Biochar improves maize growth by alleviation of nutrient stress in a moderately acidic low-input Nepalese soil. Sci. Total Environ. 625, 1380–1389.

Park, I., Tabelin, C.B., Seno, K., Jeon, S., Inano, H., Ito, M., Hiroyoshi, N., 2018. Simultaneous suppression of acid mine drainage formation and arsenic release by Carrier-microencapsulation using aluminum-catecholate complexes. Chemosphere 205, 414–425.

Park, I., Tabelin, C.B., Jeon, S., Li, X., Seno, K., Ito, M., Hiroyoshi, N., 2019. A review of recent strategies for acid mine drainage prevention and mine tailings recycling. Chemosphere 219, 588–606.

Park, I., Higuchi, K., Tabelin, C.B., Jeon, S., Ito, M., Hiroyoshi, N., 2021. Suppression of arsenopyrite oxidation by microencapsulation using ferric-catecholate complexes and phosphate. Chemosphere 269, 129413.

Podgorski, J.E., Eqani, S., Khanam, T., Ullah, R., Shen, H., Berg, M., 2017. Extensive arsenic contamination in high-pH unconfined aquifers in the Indus Valley. Sci. Adv. 3 (8), e1700935.

Preston, C.M., Schmidt, M.W., 2006. Black (pyrogenic) carbon: a synthesis of current knowledge and uncertainties with special consideration of boreal regions. Biogeosciences 3 (4), 397–420.

Rajpert, L., Kolvenbach, B.A., Ammann, E.M., Hockmann, K., Nachtegaal, M., Eiche, E., Schaffer, A., Corvini, P.F., Sklodowska, A., Lenz, M., 2016. Arsenic mobilization from historically contaminated mining soils in a continuously operated bioreactor: Implications for risk assessment. Environ. Sci. Technol. 50 (17), 9124–9132.

Rebello, S., Anoopkumar, A.N., Aneesh, E.M., Sindhu, R., Binod, P., Kim, S.H., Pandey, A., 2021. Hazardous minerals mining: Challenges and solutions. J. Hazard. Mater. 402, 123474.

Refaey, S.A.M., Taha, F., Abd El-Malak, A.M., 2004. Inhibition of stainless steel pitting corrosion in acidic medium by 2-mercaptobenzoxazole. Appl. Surf. Sci. 236 (1–4), 175–185.

Salzsauler, K.A., Sidenko, N.V., Sherriff, B.L., 2005. Arsenic mobility in alteration products of sulfide-rich, arsenopyrite-bearing mine wastes, Snow Lake, Manitoba. Canada. Appl. Geochem. 20 (12), 2303–2314.

Sharma, P., Ofner, J., Kappler, A., 2010. Formation of binary and ternary colloids and dissolved complexes of organic matter. Fe and As. Environ Sci Technol 44 (12), 4479–4485.

She, Z., Pan, X., Wang, J., Shao, R., Wang, G., Wang, S., Yue, Z., 2021. Vertical environmental gradient drives prokaryotic microbial community assembly and species coexistence in a stratified acid mine drainage lake. Water Res. 206, 117739.

Solmaz, R., Kardaş, G., Yazıcı, B., Erbil, M., 2008. Adsorption and corrosion inhibitive properties of 2-amino-5-mercapto-1,3,4-thiadiazole on mild steel in hydrochloric acid media. Colloids Surf., A 312 (1), 7–17.

Tabelin, C.B., Corpuz, R.D., Iarashi, T., Villacorte-Tabelin, M., Ito, M., Hiroyoshi, N., 2019. Hematite-catalysed scorodite formation as a novel arsenic immobilisation strategy under ambient conditions. Chemosphere 233, 946–953.

Tabelin, C.B., Silwamba, M., Paglinawan, F.C., Mondejar, A.J.S., Duc, H.G., Resabal, V.J., Opiso, E.M., Igarashi, T., Tomiyama, S., ito, M., Hiroyoshi, N., Villacorte-Tabelin, M., 2020. Solid-phase partitioning and release-retention mechanisms of copper, lead, zinc and arsenic in soils impacted by artisanal and small-scale gold mining (ASGM) activities. Chemosphere 260, 127574.

Tabelin, C.B., Park, I., Phengsaart, T., Jeon, S., Villacorte-Tabelin, M., Alonzo, D., Yoo, K., ito, M., Hiroyoshi, N., 2021. Copper and critical metals production from porphyry ores and E-wastes: A review of resource availability, processing/recycling challenges, socio-environmental aspects, and sustainability issues. Resour. Conserv. Recycl. 170, 105610.

Tay, S.L., Scott, J.M., Craw, D., 2021. Natural rehabilitation of arsenic-rich historical tailings at the Alexander mine, Reefton, New Zealand. New Zeal. J. Geol. Geop. 64 (4), 558–569.

Tu, Z., Wan, J., Guo, C., Fan, C., Zhang, T., Lu, G., Reinfelder, J.R., Dang, Z., 2017. Electrochemical oxidation of pyrite in pH 2 electrolyte. Electrochim. Acta 239, 25–35.

Veselska, V., Sillerova, H., Hudcova, B., Ratie, G., Lacina, P., Lalinska-Volekova, B., Trakal, L., Sottnik, P., Jurkovic, L., Pohorely, M., Vantelon, D., Safarik, I., Komarek, M., 2022. Innovative in situ remediation of mine waters using a layered double hydroxide-biochar composite. J. Hazard. Mater. 424, 127136.

Wang, S., Zheng, K., Li, H., Feng, X., Wang, L., Liu, Q., 2021. Arsenopyrite weathering in acidic water: Humic acid affection and arsenic transformation. Water Res. 194, 116917.

Xu, J., Yin, Y., Tan, Z., Wang, B., Guo, X., Li, X., Liu, J., 2019. Enhanced removal of Cr (VI) by biochar with Fe as electron shuttles. J. Environ. Sci.-China 78 (4), 109–117.

Yaashikaa, P.R., Senthil Kumar, P., Varjani, S.J., Saravanan, A., 2019. Advances in production and application of biochar from lignocellulosic feedstocks for remediation of environmental pollutants. Bioresour. Technol. 292, 122030.

Yang, B., Luo, W., Wang, X., Yu, S., Gan, M., Wang, J., Liu, X., Qiu, G., 2020. The use of biochar for controlling acid mine drainage through the inhibition of chalcopyrite biodissolution. Sci. Total Environ. 737, 139485.

Zhang, D.R., Chen, H.R., Xia, J.L., Nie, Z.Y., Zhang, R.Y., Schippers, A., Shu, W.S., Qian, L.X., 2021. Red mud regulates arsenic fate at acidic pH via regulating arsenopyrite bio-oxidation and S, Fe, Al. Si speciation transformation. Water Res. 203, 117539.

Zhang, M., Song, G., Gelardi, D.L., Huang, L., Khan, E., Masek, O., Parikh, S.J., Ok, Y.S., 2020a. Evaluating biochar and its modifications for the removal of ammonium, nitrate, and phosphate in water. Water Res. 186, 116303.

Zhang, K., Sun, P., Faye, M.C.A.S., Zhang, Y., 2018. Characterization of biochar derived from rice husks and its potential in chlorobenzene degradation. Carbon 130, 730–740.

Zhang, Y., Zhao, H., Qian, L., Sun, M., Lv, X., Zhang, L., Petersen, J., Qiu, G., 2020b. A brief overview on the dissolution mechanisms of sulfide minerals in acidic sulfate environments at low temperatures: Emphasis on electrochemical cyclic voltammetry analysis. Miner. Eng. 158, 106586.

Zheng, K., Li, H., Wang, S., Feng, X., Wang, L., Liu, Q., 2020. Arsenopyrite weathering in sodium chloride solution: Arsenic geochemical evolution and environmental effects. J. Hazard. Mater. 392, 122502.